Available online at www.sciencedirect.com
SCIENCE DIRECT®
Journal of Nuclear Materials 347 (2005) 178–191
journal of nuclear materials
www.elsevier.com/locate/jnucmat

Threats, design limits and design windows for laser IFE dry wall chambers

A. René Raffray *, The HAPL Team

Mechanical and Aerospace Engineering Department, Center for Energy Research, University of California, San Diego, 458 EBU-II, La Jolla, CA 92093-0438, USA

Abstract

The High Average Power Laser (HAPL) program is carrying out a coordinated effort to develop inertial fusion energy based on lasers, direct-drive targets and a dry wall chamber. The dry wall must accommodate the ion and photon threat spectra from the fusion micro-explosion over its required lifetime. This paper summarizes the current HAPL strategy on the armor/first wall configuration based on tungsten and ferritic steel as preferred armor and structural materials, respectively. The thermal performance of an example fully dense tungsten armor configuration on a ferritic steel first wall is described showing the basis for separating the high energy accommodation function of the armor from the structural function of the first wall. Example design operating windows for the armor, first wall and blanket are presented based on different requirements and constraints. The possibility of utilizing an engineered porous armor is discussed. Key chamber wall and armor issues are summarized.

1. Introduction

The High Average Power Laser (HAPL) program [1] is carrying out a coordinated, focused effort to develop laser inertial fusion energy (laser IFE) based on lasers, direct-drive targets and a dry wall chamber. The dry wall must be designed to accommodate the cyclic and intense photon and ion energy deposition from the fusion micro-explosion while providing the required lifetime. Most of the photon and ion energy deposition occurs within a short penetration depth in the first wall (10–100 μm) which experiences highly pulsed conditions. The neutron energy is deposited deeper in the first wall and blanket and does not represent a major threat to first wall survival. As such, it seems prudent to design for a thin armor attached to a structural first wall. This provides for separation of functions and the thin armor can be optimized to accommodate the photon and ion threat spectra while the first wall is optimized for structural and heat removal functions.

Candidate dry chamber armor materials must have high temperature capability and good thermal properties for accommodating the energy deposition and providing the required lifetime. The armor interfaces with the first wall and blanket and there

* Tel.: +1 858 534 9720; fax: +1 858 822 2120.
E-mail address: raffray@fusion.ucsd.edu

0022-3115/$ - see front matter © 2005 Elsevier B.V. All rights reserved.
doi:10.1016/j.jnucmat.2005.08.015

must be compatibility between the choice of armor material and the choice of structural material, coolant and blanket configuration. To help focus the resources on the materials with the highest probability of success within the proposed time frame, the HAPL laser IFE community has decided to concentrate on a first wall concept based on tungsten as preferred armor material and ferritic steel as structural material. This also allows for the possible use of a number of compatible blanket designs which are being developed for magnetic fusion energy (MFE) applications; thus, the limited IFE R&D resources can be directed to solving the IFE-specific armor/first wall issues, while maximum use can be made of all the information available from the large MFE effort on blankets.

It is recognized that the design studies of the armor and first wall, and of the blanket and coupled power cycle should be integrated at an early stage since many design and operating parameters of these components are interdependent. In addition to a conventional fully dense tungsten layer as armor material, the possibility of utilizing engineered tungsten as armor is being considered to promote implanted helium release and possibly to better accommodate peak thermal stresses. Proposed armor configurations include a foam structure, described in detail in Ref. [2], and a plasma-sprayed nano-sized porous structure [3]. These porous regions would be very thin and would be bonded to a fully dense tungsten, itself bonded to the ferritic steel first wall. They would also have to provide acceptable thermal performance under the high energy deposition from the photon and ion threat spectra.

This paper covers the current HAPL design strategy for the chamber. The threats from the fusion micro-explosion are first described. The thermal performance of an example fully dense tungsten armor configuration on a ferritic steel first wall is then described and associated issues are then discussed including the impact of temperature-related material limits on operating parameters. The interdependence of the armor, first wall, blanket and cycle design is then illustrated through an example parametric analysis from which operating windows can be evolved from different requirements and constraints. The possibility of using a porous 'engineered' armor is then assessed in terms of its thermal performance under the ion and photon energy deposition with the aim of helping to narrow down the most desirable porous micro-structure characteristics. Finally, the major observations and conclusions from this study are summarized.

2. Threats

The 154 MJ NRL direct-drive target shown in Fig. 1 [4,5] was used as the base target for the analysis presented in this paper. The energy partitioning from this target, estimated from LASNEX calculations [6], is shown in Table 1 [6]. The major threats to the chamber wall are the ions which carry about 28% of the energy and, to a lesser extent (thermally), the photons which carry about 1% of the energy. Neutrons penetrate much deeper in the structure and blanket and as such are much lesser threat to the chamber wall. The photon spectrum is shown in Fig. 2 while the burn products (fast ions) and debris ions spectra for the 154 MJ direct-drive target are shown in Figs. 3 and 4, respectively. Higher yield direct-drive targets are also considered in the study but their energy partitioning and ion and photon spectra tend be similar to those for the 154 MJ target; for the purpose of analysis, the relative energy partitioning and threat spectra from the 154 MJ target are used as representative of targets with different yields, with the energy levels being scaled accordingly.

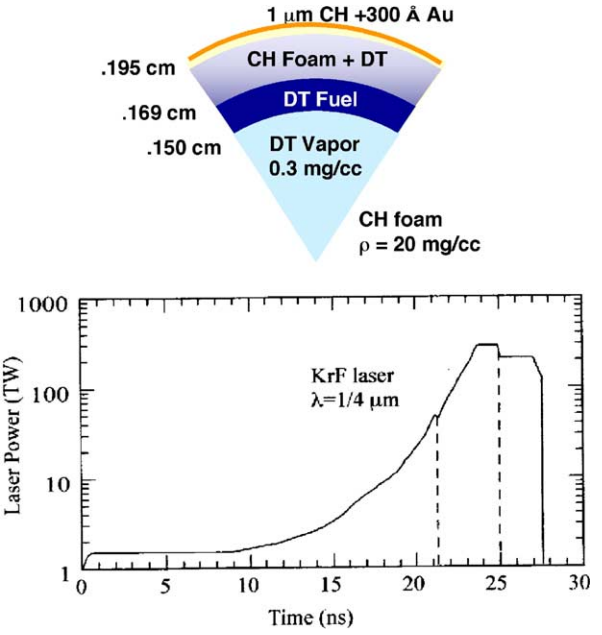

Fig. 1. Example direct-drive target (NRL) to be coupled with a laser driver [4,5].

Table 1
Energy partitioning for 154 MJ NRL direct-drive target [6]

	NRL direct-drive target (MJ)
X-rays	2.1 (1.4%)
Neutrons	109 (71%)
Gammas	0.009 (0.006%)
Burn product fast ions	19.5 (13%)
Debris ions kinetic energy	22.1 (14%)
Residual energy	1.29
Total	154

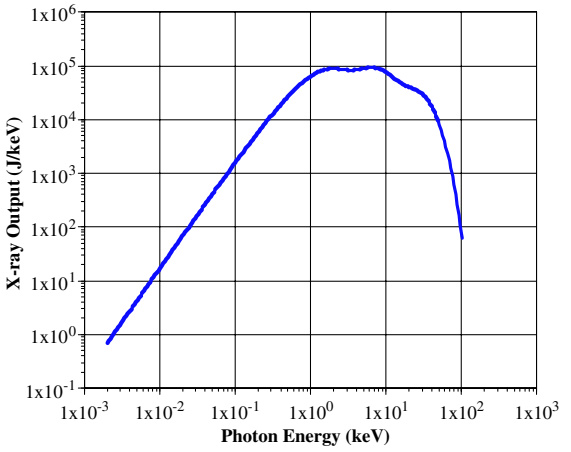

Fig. 2. Photon spectra from NRL 154 MJ direct-drive target [6].

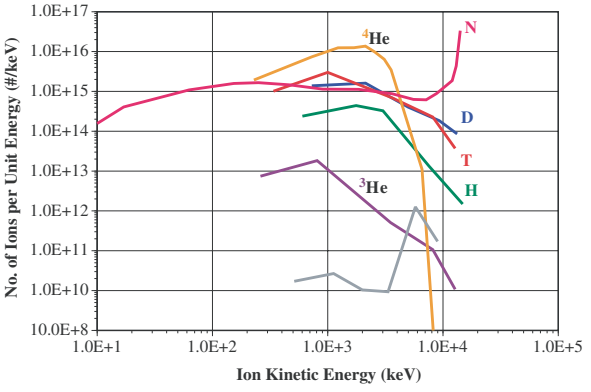

Fig. 3. Fast ion spectra from NRL 154 MJ direct-drive target [6].

3. Armor/first wall material and configuration choices, design and constraints

Candidate dry chamber armor materials must have high temperature capability and good thermal properties for accommodating energy deposition and providing the required lifetime. A refractory

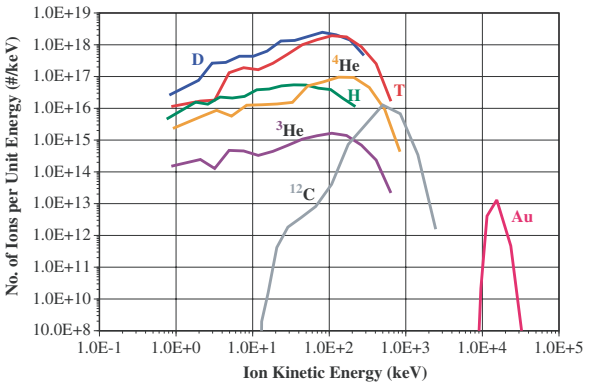

Fig. 4. Debris ion spectra from NRL154 MJ direct-drive target [6].

metal, such as tungsten, is an attractive candidate in this respect. Also, there are no major trapping mechanisms of the tritium flux to the wall and tritium inventory in a W armor is not of particular concern. However, lifetime is an issue that needs to be addressed. It includes: (i) the possibility of melting and whether this should be avoided; (ii) the thermo-mechanical response of the surface to the cyclic temperature gradients (which could lead to roughening or fracture); and (iii) whether the implanted He ions can be released to avoid premature armor failure due to He accumulation [7]. It is believed that these issues can be addressed through material selection (including the possibility of utilizing an 'engineered' porous armor surface for stress relief and/or He release enhancement [2]) and a focused R&D program.

Carbon is a good armor candidate based on its high temperature capability and has been considered in previous studies (e.g. [8]). Also, as shown in Section 4, the ion and photon penetration depths are longer in carbon than in tungsten, spreading the energy deposition over a larger volume. However, several mass loss processes have been identified in carbon including chemical erosion and radiation enhanced sublimation which lead to serious concerns of lifetime and tritium inventory through co-deposition in cold regions; in addition, concerns exist about the properties of carbon under high temperature and irradiation [7]. Thus, it is believed that carbon would require substantially more R&D than tungsten. For illustrative purposes, typical properties are tungsten and carbon are summarized in Table 2 [7].

Low-activation ferritic (LAF) steel was selected as structural material. Given the need to field the

Table 2
Summary of tungsten and carbon armor material properties [7]

Thermo-physical properties	Tungsten	Carbon[a]
Density (kg/m^3)	~19 350	~2000
Phase change temperature (K)	3683 (melting)	3640 (sublimation)
Thermal conductivity (W/m K)	148 (500 K) 90 (3000 K)	90 (573 K)[b] 213 (>1500 K)
Specific heat (J/kg K)	138 (500 K) 225 (3000 K)	1350 (500 K) 2450 (3000 K)
Heat of fusion (kJ/kg)	192	–
Heat of vaporization (kJ/kg)	4009	59 400[c]
Molecular weight	183.85	12
Vapor pressure (Pa)	$= 10^{12.74-\frac{44\,485}{T\,(\mathrm{K})}}$	$= 10^{15.75-\frac{40\,750}{T\,(\mathrm{K})}}$

[a] A thin CVD carbon armor is assumed over a carbon–fiber-composite structure.
[b] Thermal conductivity of neutron irradiated MKC-1PH CFC (1 dPa).
[c] This value is based on sublimation of mono-atomic carbon, C_1.

concept within 12–15 years, it seems to be the material with enough development maturity to minimize the risk in utilizing it while providing an acceptable operating temperature window for power plant performance (cycle efficiency). Oxide-dispersion strengthened (ODS) or nano-composited steel is considered as an alternate LAF structure as it would allow for a higher temperature of operation and possibly better bonding with tungsten. However, its data base is more limited and the practical aspects of its application such as forming and bonding will require greater R&D than the conventional LAF's. Other structural materials (such as the higher performance but higher risk SiC_f/SiC composites) could be considered in the future if justified then by advances in R&D.

The major armor and first wall challenges include armor material type (e.g. W alloy and possible engineered structure), bonding to LAF, lifetime and general suitability of W/Fe in an overall fusion/nuclear system. These issues are being addressed through the HAPL R&D program and are described in more details in Refs. [1,9]. Some armor-relevant information can also be learned from the MFE effort on plasma material interaction (including tungsten) since although MFE strives for steady state conditions, there are some dynamic scenarios (such as edge localized mode scenarios) where the armor experiences conditions closer to those associated with cyclic IFE operations [7]. This provides for possible synergy between the MFE and IFE R&D program on armor.

The results from the R&D effort will help in deriving better limits on operating conditions of the armor/FW based on integrity and lifetime requirements. For example, it is not clear what the maximum acceptable temperature (or temperature change) limit should be for the tungsten armor. It is possible that cyclic thermal stresses due to the high power deposition would cause cracks or roughening in the armor but this might be acceptable if they saturate. It is certainly unacceptable to have crack propagation through the tungsten/ferritic steel interface as this will affect the first wall lifetime but the conditions under which this might occur are not yet well characterized. Even if tungsten is allowed to operate at a temperature approaching its melting point (3410 °C), it is not clear whether total melt avoidance would be required as this would depend on the stability of the melt layer and on the material form and integrity following re-solidification. Results of the experimental R&D in facilities with different cyclic heat sources (ions, X-rays, laser) will greatly help in understanding the different phenomena taking place and their dynamic behavior over large number of cycles at different temperature levels. More accurate limits could then be set for the different tungsten configurations (e.g. alloys and/or engineered structure). Here, for the illustrative purpose of the parametric studies presented in Section 6, a maximum temperature limit of 2400 °C is assumed for tungsten based on some preliminary roughening results for tungsten [10].

For ferritic steel as structural material, operating limits are relatively well understood based on the MFE material community's effort [11]. Stress-based constraints would require the local stress level to be within the maximum allowable stress at the given temperature. Ideally, to accurately impose such a limit would require a detailed thermo-mechanical analysis. For the purpose of this paper, a general guideline is assumed, limiting the ferritic steel temperature to <550 °C. This temperature limit would be extended to ~700 °C in the case of ODS ferritic steel but with the recognition that joining of this material is problematic [11]. In addition, depending on the coolant, compatibility constraints would also limit the FS/coolant interface temperature; for example, for lithium as coolant the maximum interface temperature is limited to ~600 °C [11].

4. Photon and ion energy deposition in armor

The photon and ion energy deposition in the armor was calculated based on a 1-D slab geometry. An attenuation calculation was used for the photon energy deposition based on data for the attenuation coefficient in the material (including photo-electric and Compton scattering effects) as a function of the photon energy [12]. The ion deposition calculation included both the electronic and nuclear stopping powers which were obtained as a function of ion energy from SRIM [13]. The calculations proceeded by following ions at discretized energy levels from the spectra though the material slab. Fig. 5 shows the energy deposition as a function of penetration depth for W for the 154 MJ direct-drive target spectra assuming a chamber radius of 6.5 m and no protective gas in the chamber. For completeness and to illustrate the difference between low-Z and high-Z materials, the energy deposition in carbon is also shown in the figure. These results can be scaled to the yield to estimate the energy deposition for targets of different yields.

The calculation procedure included the time of flight spreading of the photon and ion energy deposition following the micro-explosion. The photons travel much faster than the ions and would reach the chamber wall within about 20 ns over a time spread of sub-ns. The ions take longer to reach the chamber wall and would reach the wall at different times depending on their energy, thereby spreading the energy deposition over time and lowering the peak heat generation in the wall. This is a key effect which needs to be included as assumption of instantaneous energy deposition can close the design window for dry wall or necessitate radical measures such as the use of much larger chamber and/or much higher buffer gas density in the chamber to protect the armor. As an example, the ion power deposition in a tungsten armor is shown in Fig. 6 as a function of time after the micro-explosion and penetration depth for the 154 MJ NRL direct-drive target in a chamber of radius 6.5 m with no protective gas. The initial power deposition from the photons occurring within the first 20 ns is not shown in this figure. The figure illustrates the spread in heat generation with most of the fast ion power deposition occurring within a fraction of a μs whereas most of the slow ion power deposition occurs within ~2 μs. The highest heating volumetric heat generation in the tungsten is about 4.5×10^{16} W/m^3 occurring after about 1.5 μs and is due to the slow ion energy deposition.

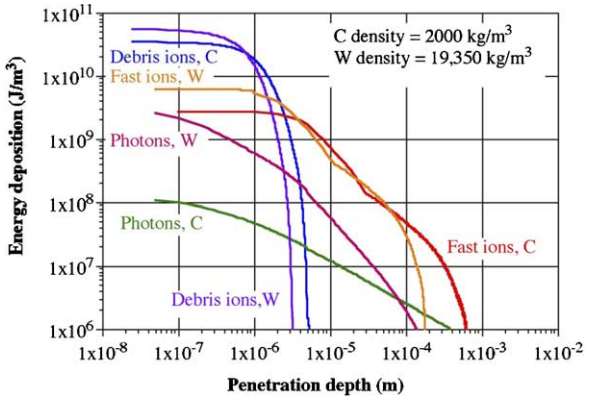

Fig. 5. Energy deposition as a function of penetration depth for C and W for the 154 MJ direct-drive target spectra assuming a chamber radius of 6.5 m and no protective gas in the chamber.

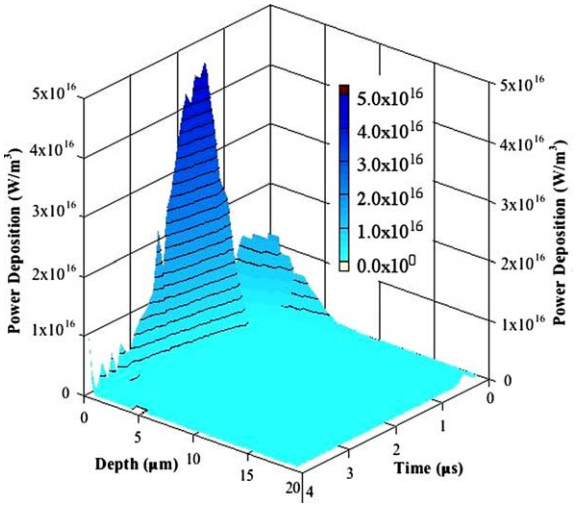

Fig. 6. Ion power deposition in tungsten armor as a function of time and penetration depth for the 154 MJ NRL direct-drive target and assuming a chamber radius of 6.5 m with no protective gas.

5. Fully dense tungsten armor/FW thermal behavior

The volumetric heat generation data described in the previous section was used as input to analyze the thermal behavior of the armor and first wall. Temperature-dependent properties were utilized for W (see Table 2). Calculations for cases with no protective chamber gas were performed using a modified version of RACLETTE, the 1-D thermal analysis

code with phase change modeling capability [14]. In this code, melting is modeled by changing the enthalpy of the material over about one degree at the melting point to account for the latent heat of fusion, and evaporation is modeled by calculating the evaporated flux as a function of the wall temperature and then multiplying by the latent heat of evaporation to calculate the effective heat flux [14,7].

For cases with a protective gas, BUCKY [15] an integrated 1-D code calculating the photon and ion energy deposition and the wall thermal response was first used parametrically to provide the attenuation of the initial ion and photon energy deposition as a function of chamber size and chamber gas density. The attenuated energy is then re-radiated over a somewhat longer time scale (200–700 μs). Thus, the attenuation would greatly help in reducing the temperature and temperature gradient of the armor close to the surface but would not much affect the heat flux at the W/FS interface or beyond for armor thicknesses of ~0.2 mm or higher since the time constant for thermal diffusivity through the armor (e.g. ~1.6–40 μs for armor thicknesses of ~0.2–1 mm) is significantly longer than the re-radiation time. Example energy deposition attenuation factors from BUCKY are shown in Table 3 [16]. These can then be used as input in RACLETTE for simple parametric analyses of the initial armor thermal behavior as a function of chamber size and gas density.

For these analyses, a simple armor/FW configuration is assumed, consisting of a thin tungsten armor layer of varying thicknesses (0.1–3 mm) bonded to a FS structural first wall with the coolant running on its other side. The coolant temperature and heat transfer coefficient at the FW/coolant interface would affect the overall temperature level of the armor/FW but not the dynamic behavior of the armor. For the initial parametric analyses, the coolant temperature was set at 500 °C and the heat transfer coefficient at 10 kW/m^2 K with the understanding that the overall temperature level could be adjusted by changing these coolant parameters.

Table 3
Attenuation of initial ion and photon energy deposition on armor as a function of chamber gas density for a chamber of radius 6.5 m [16]

Gas density (mTorr at 300 K)	10	20
Reduction in initial photon intensity on the wall	9%	16%
Reduction in initial burn product fast ions energy deposition on the wall	1%	2%
Reduction in initial debris ions energy deposition on the wall	29%	48%
Re-radiation time scale (μs)	300–700	300–700

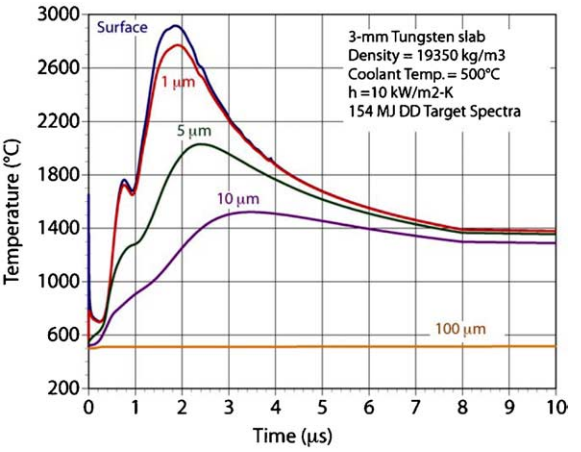

Fig. 7. Temperature history at different locations in a 3-mm W slab without a protective gas exposed to the 154 MJ direct-drive target threat spectra in a chamber of radius 6.5 m and with a coolant temperature of 500 °C.

Example results for a single shot scenario (for the 154 MJ target) are summarized in Fig. 7 for an initial case with a thick armor slab (3 mm) without a protective gas exposed to the 154 MJ direct-drive target threat spectra in a chamber of radius 6.5 m. The photon energy deposition is very fast and creates the instantaneous temperature increase of about 1650 °C shown in the figure. The maximum W temperature is about 2900 °C in this case. Note that this temperature would be unacceptable based on the limit of about 2400 °C assumed for the example parametric studies in the next section. However, this limit is very approximate and will need to be better defined based on the results from the ongoing experimental and modeling R&D effort. From the figure, only a very thin armor region (<100 μm) sees the initial temperature transient.

Multi-shot analyses of the FW/armor configuration were also performed and are illustrated in the example cases shown in Figs. 8 and 9, for a repetition rate of 10. Fig. 8 shows the maximum armor temperature history over a number of shots for a 0.5-mm thick armor bonded to a 2.5-mm thick FS structural wall subject to the 154 MJ direct-drive target threat spectra in a chamber of radius 6.5 m without a protective gas and with a coolant temperature of 500 °C. The maximum armor temperature during the first shot is about 2900 °C, about the same as for the 3-mm armor case shown in Fig. 7. Fig. 9 shows the corresponding ferritic steel temperature histories at

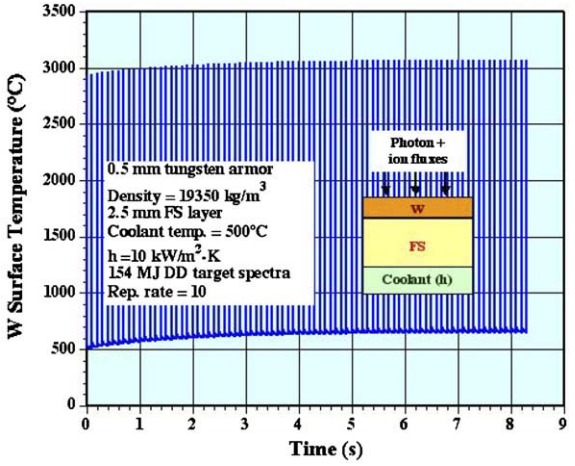

Fig. 8. Maximum tungsten armor temperature history over a number of shots for a 0.5-mm thick armor without a protective gas exposed to the 154 MJ direct-drive target threat spectra in a chamber of radius 6.5 m and with a coolant temperature of 500 °C.

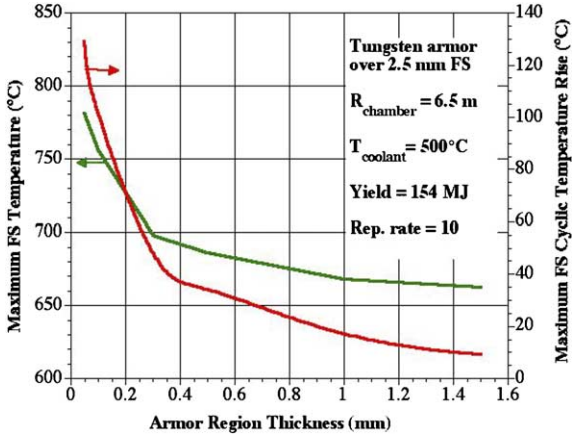

Fig. 10. Maximum temperature and maximum temperature swing at the FS/W interface as a function of armor thickness for a W armor bonded to a 2.5-mm thick FS structural wall subject to the 154 MJ direct-drive target threat spectra in a chamber of radius 6.5 m without a protective gas and with a coolant temperature of 500 °C.

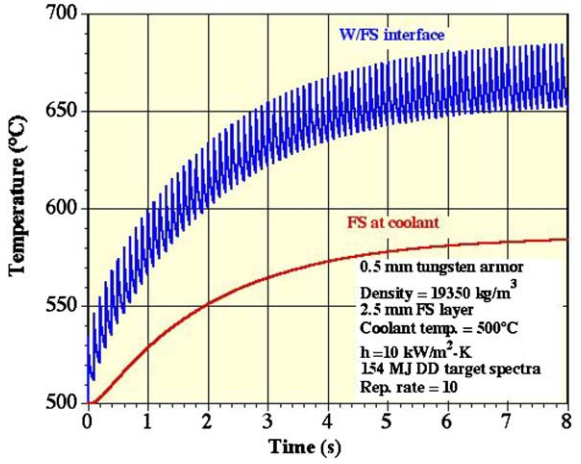

Fig. 9. Ferritic steel temperature histories at the W/FS and coolant interfaces, respectively, for a 0.5-mm thick armor bonded to a 2.5-mm thick FS structural wall subject to the 154 MJ direct-drive target threat spectra in a chamber of radius 6.5 m without a protective gas and with a coolant temperature of 500 °C.

the W/FS and coolant interfaces, respectively. From both figures, it can be seen that a quasi-steady-state is reached fairly rapidly, within about 100 shots or less. From Fig. 9, the FS temperature at the coolant is constant once steady state conditions are reached. However, the FS temperature at the FS/W interface undergoes a small temperature swing of about 34 °C for this thickness of armor. Parametric analyses with different thicknesses of armor confirms that the armor thickness has a minimal effect on the maximum tungsten armor temperature but indicates that it can strongly influence the maximum FS temperature and cyclic temperature swing at the W/FS interface, as shown in Fig. 10.

These results confirm the design basis for separation of functions, with a thin armor providing the high energy accommodation function bonded to a FS substrate providing the structural function and interfacing with the coolant and blanket which effectively see quasi-steady-state conditions. The armor region thickness should be set in coordination with the coolant temperature and film drop to ensure that the FS maximum temperature stays within the maximum allowable limit. For example, from Fig. 10, the FS maximum temperature is about 662 °C for an armor region thickness of 1.5 mm. This would be acceptable if ODS FS is used (max. temp. limit ~ 700 °C). However, if regular FS is used (max. temp. limit ~ 550 °C), then a thicker armor or a lower coolant temperature would be needed. The armor thickness also determines the temperature swing at the FS/W interface. The exact temperature swing allowed there would have to be determined through detailed fatigue calculations. As a conservative preliminary guideline, it seems prudent to set the armor thickness in order to minimize the cyclic thermal stress (and, hence, the cyclic temperature swing) at the FS/W interface. For example an armor thickness of 1.5 mm or more would limit the temperature swing at the FS/W

interface to about 10 °C or less. However, the selected armor thickness would also need to accommodate the maximum W temperature limit for the given coolant conditions and would need to be compatible with demonstrated fabrication methods.

6. Example design windows for first wall, blanket and power cycle

The armor/first wall, blanket and cycle design and optimization must be integrated as their parameters are interrelated. For example, the choice of a power cycle would depend on its compatibility with the blanket coolant and on the maximum coolant temperature. A Brayton cycle provides higher efficiency than a Rankine cycle but requires a higher coolant temperature. However, if, for instance, lithium is used as blanket coolant, it would be highly desirable to avoid the possibility of lithium/steam reaction. Achievable performance would then have to be balanced against safety considerations, and a Brayton cycle would probably be preferred to a Rankine cycle even at the cost of slightly lower performance.

The achievable cycle efficiency is dependent on the blanket coolant outlet and inlet temperatures, as illustrated below for the example Brayton cycle configuration shown in Fig. 11. This configuration comprises three compressor stages (low pressure, LP; intermediate pressure, IP; and high pressure, HP), two intercoolers and a single expansion stage (including a split-shaft turbine to allow independent optimization of compressor and turbine aerodynamic performance) [17]. The energy from the blanket coolant is transferred to the cycle He through a heat exchanger (HX). The efficiency of this cycle was estimated for example parameters (including a compressor efficiency, $\eta_C = 0.89$; a turbine efficiency, $\eta_T = 0.93$; a recuperator effectiveness, $\varepsilon_{rec} = 0.95$ and a cycle pressure drop ratio, $\Delta P/P_{high} = 0.05$). The cycle efficiency is dependent on the total compression ratio, as illustrated in Fig. 12 for a

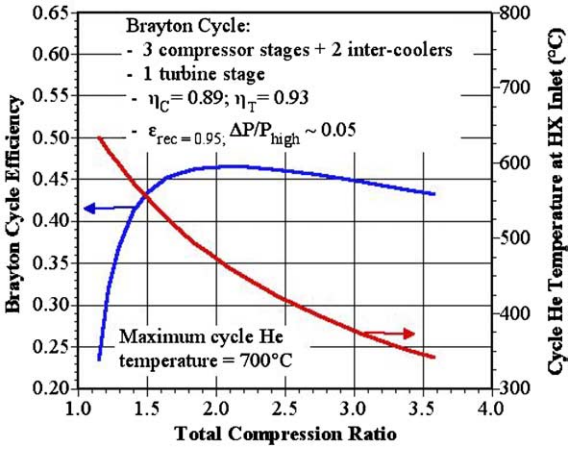

Fig. 12. Brayton cycle efficiency as a function of total compression ratio for a maximum cycle He temperature of 700 °C. The corresponding cycle He temperature at the entry to the heat exchanger is also shown.

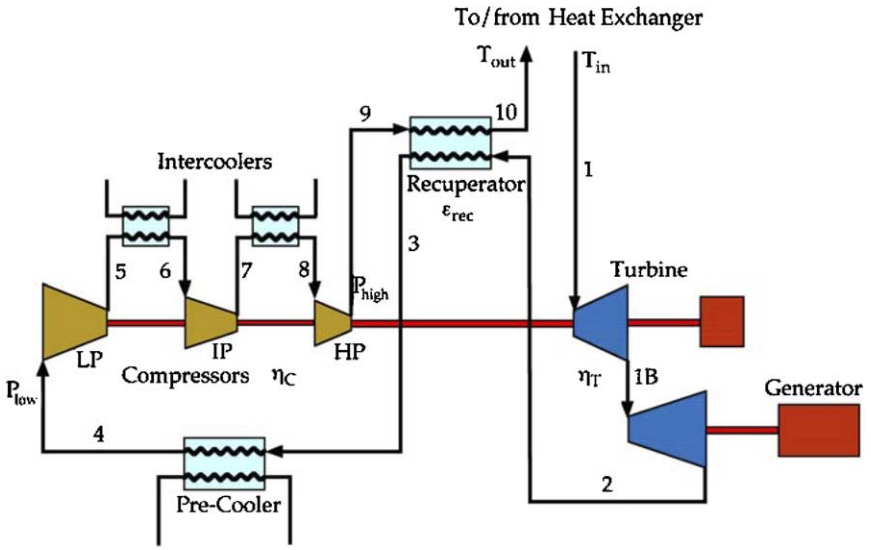

Fig. 11. Example Brayton cycle configuration.

maximum cycle He temperature of 700 °C (at the heat exchanger outlet). The efficiency peaks at about 46.5% for a total compression ratio of about 2. The figure also shows the corresponding cycle He temperature at the entry to the heat exchanger, which decreases significantly with increasing compression ratio. The maximum cycle efficiency was calculated as a function of the maximum cycle He temperatures (for optimum compression ratio in each case) and the results are summarized in Fig. 13. The figure also shows the cycle He temperature at the entry to the heat exchanger corresponding to the optimized values of compression ratio.

For a given temperature drop between the heat exchanger fluids, the cycle He temperatures at the heat exchanger entry and exit set the corresponding blanket coolant temperatures on the other side of the heat exchanger; thus, the results clearly illustrate the importance of optimizing the combination of blanket outlet and inlet temperatures to maximize the cycle efficiency. However, when integrated with the first wall and blanket design, the optimum combination of inlet and outlet coolant temperatures (maximizing the cycle efficiency) might not be acceptable based on maximum material temperature limits. Thus, an integrated cycle optimization including first wall and blanket constraints is required.

Since the blanket sees essentially steady state operation except for the neutron pulses, the HAPL strategy is to utilize information from the MFE blanket effort in developing FW/Blanket concepts

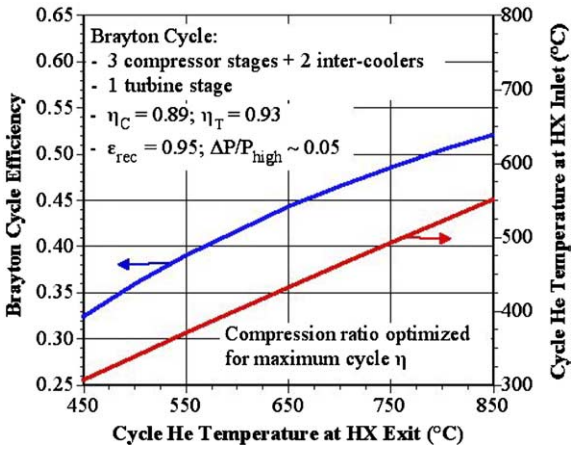

Fig. 13. Brayton cycle efficiency as a function of maximum cycle He temperature (at outlet of heat exchanger) for optimized values of the compression ration. The corresponding cycle He temperature at the entry to the heat exchanger is also shown.

compatible with FS as structural material and W as armor material (e.g. [18]). A two-phase strategy has been envisioned: a scoping phase and a detailed design analysis phase (each covering about a year). During the current first phase, a number of blanket concepts (2–4) are being developed to the point where they can be intelligently evaluated in terms of key issues including performance, reliability, simplicity, and safety. This assessment would allow a convergence on one or two preferred design concepts which will then be analyzed more thoroughly during the second phase to cover all the key aspects: fabrication, operation, maintenance and integration, and to end up with a strongly-credible and attractive integrated design.

The choice of possible blanket materials concerns essentially the breeder and coolant since the structural (FS) and armor (W) materials have already been selected. Most recent MFE blanket designs have diverged away from using water as coolant for different reasons including low performance and compatibility problems with different materials (structural, breeding and/or coolant). Potentially attractive blanket concepts for IFE covering a good range of performance and potential risk, include: (i) self-cooled Li; (ii) He-cooled ceramic-breeder; (iii) He-cooled or dual cooled Pb–17Li; and (iv) dual cooled molten salt (with He as FW coolant).

Fully self-cooled Pb–17Li and/or molten salt (flibe) blankets could also be considered but their rather poor heat transfer performances (for flibe even more than for Pb–17Li) make it very difficult to provide accommodation of the heat fluxes and material constraints with reasonable performance (cycle efficiency) and power densities. In addition the rather low compatibility temperature limit for Pb–17Li/FS could be overly constraining.

The scoping study of the first concept (self-cooled Li) has concluded and this is the concept which is used as example here with the clear understanding that the blanket scoping studies are continuing and no reference design has been selected yet. This is an interesting concept when applied to IFE (as contrasted to MFE) since the absence of magnetic field allows the designer to take advantage of the high heat transfer capability of lithium without the MHD issue. Fig. 14 illustrates the concept, described in more detail in Ref. [19]. It consists of banks of vertically-arranged rectangular tubes (or submodules) extending the whole height of the nearly cylindrical chamber. The first wall of the submodule consists of a 0.35-cm thick layer of ferritic

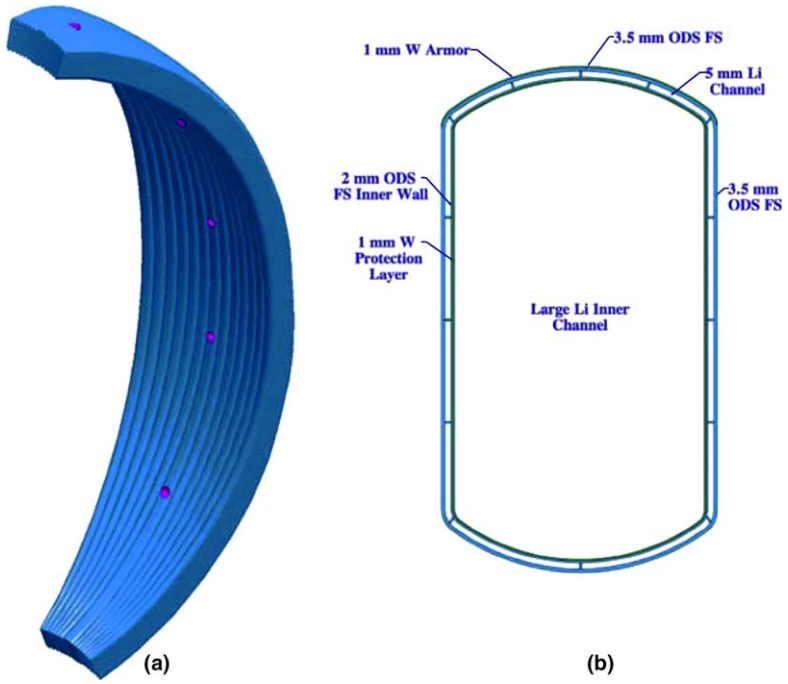

Fig. 14. Schematic of self-cooled Li concept for HAPL showing: (a) arrangement of a number of submodules on one side of the chamber; and (b) a cross-section of a submodule at the midplane of the chamber [19].

steel, which has a 0.1-cm thick tungsten armor layer diffusion bonded to it. The rectangular tubes vary in width and depth to accommodate the shape of the chamber. Concentric with the outer tube, is another inner tube floating inside the submodule and separated from the outer wall to form an annular channel. The outer wall (including the first wall) is cooled with Li which is admitted at the bottom of the blanket, flows through the annular gap to the top and then returns to the bottom at low velocity through the large center channel provided by the second concentric tube. This allows to some extent the decoupling of the lithium outlet temperature from the wall temperature. One of the early parametric studies of this blanket looked at the constraint posed by the 600 °C compatibility limit at the lithium/FS interface at the outlet of the first wall channel (assuming that the FS maximum temperature limit was higher, e.g. ~700 °C for ODS FS). The coolant temperature at the outlet of the first wall is constrained to a value corresponding to this compatibility limit (600 °C) minus the film temperature drop (given by the local heat flux divided by the coolant convective heat transfer coefficient). For a heat flux corresponding to 1800 MW fusion power and for an example set of thermal-hydraulic parameters of the lithium flow in the annular channel, these initial results indicated that the coolant temperature at the outlet of the first wall was constrained to ~570–580 °C for chamber radii of 5.7 m or higher [20]. For corresponding inlet and outlet temperatures of the Li in the blanket of about 450 °C and 740 °C, respectively, the Brayton cycle efficiency is about 46% (for an assumed temperature drop of 50 °C between the heat exchanger fluids) [20].

These blanket and cycle analysis results can be integrated to the armor and first wall analysis performed with RACLETTE by setting appropriate values of the lithium temperature and heat transfer coefficient at the first wall channel outlet. Admittedly, these conditions would change somewhat based on the first wall channel geometry and Li flow rates but the changes should be small (of the order of ~10 °C) and should have a minor effect on the overall presentation of the results. From the W armor, as mentioned in Section 3, a maximum temperature of 2400 °C is assumed as limit for these example trade-off studies. Fig. 15 summarizes the results for a fusion power of 1800 MW, and FS first wall and W armor thicknesses of 3.5 and 1 mm, respectively. The coolant temperature and heat transfer coefficient were set at 572 °C and 67 kW/m^2 K, respectively. The dashed lines show the combination of chamber gas density (in terms of

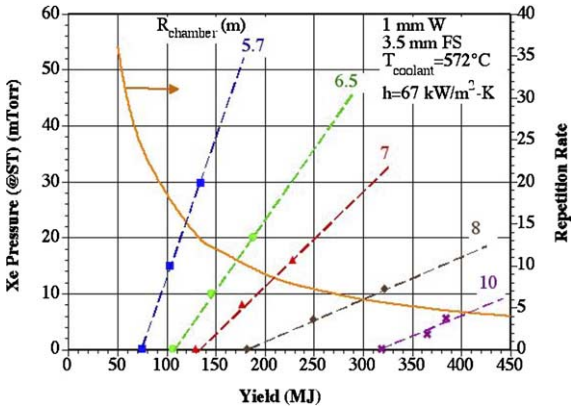

Fig. 15. Example integrated parametric study showing combinations of chamber gas density, yield and chamber size that would maintain the W armor temperature <2400 °C for a fusion power of 1800 MW and a coolant temperature of 572 °C.

pressure at 300 K) and target yield that would limit the armor temperature to 2400 °C for different chamber radii. The calculations used the attenuation coefficients from Table 3 in estimating the attenuating effect of the chamber gas on the initial photon and ion energy depositions. The analysis for varying yields was performed by scaling the energy deposition from the 154 MJ target to the yield. Essentially the same figure would be obtained for different fusion power levels, except that the lines will be shifted somewhat to reflect the change in coolant temperature and heat transfer coefficient.

From the figure, for this example, for a target yield of about 150 MJ, no protective gas would be required in a chamber of radius ~7.5 m. For a smaller chamber, ~7 m in radius, no protective gas would be required for a target yield of ~130 MJ. The same chamber would be able to accommodate up to a ~350 MJ target with ~35–40 mTorr of Xe as protective gas. For a case with no protective gas, a larger chamber (10–11 m) would be required to accommodate such a yield (350 MJ). Since the fusion power is fixed, the repetition rate corresponding to the yield is shown on the second vertical axis and is represented by the solid line. For a fully integrated study other constraints would have to be included in the figure, such as laser and target requirements on the maximum allowable chamber gas density for a given chamber size [21]. For example, under high chamber gas density the laser beam may not focus on the target and/or the variation of the laser intensity on the target may become unacceptably large. The only experimental data available for laser beam propagation and focusing in an IFE chamber is from NIKE experiment. In these experiments, modest changes in the response of the planar targets were observed when the Xe pressure was raised above 200 mTorr [21]. As shown in Fig. 15, such an upper bound on the chamber gas density (off scale in the figure) provides a comfortable margin for the chamber wall operating design window.

The target survival requirements on the chamber gas density can be far more restrictive. Target heating from energy exchange with the background gas during injection is limited to maintain the level of symmetry and smoothness required from target physics consideration [22,23]. It is not clear yet what this limit may be but initial studies have assumed that the DT should be maintained below its triple point. For the base target, shown in Fig. 1, at an initial temperature of 18 K, a heat flux of ~6000 W/m^2 would cause the DT to reach its triple point (~19.79 K) assuming an injection velocity of 400 m/s and a chamber of radius 6 m. This is a very low value when considering the heat sources from chamber wall radiation and chamber gas energy exchange. For example, even with a reflectivity of ~96% for the very thin reflective coating (0.275–0.375 μm) on the target, such a heat flux could result from radiation alone for a wall temperature of 1275 K. However, radiation heat flux can be controlled to some extent by running the coolant and the wall at lower temperature (500–600 °C). Based on heating from chamber gas energy exchange only, such a limit (6000 W/m^2) would restrict the effective chamber gas density to $\sim 7 \times 10^{19}$ atoms/m^3 of Xe at 4000 K in the 6 m chamber (corresponding to ~2 mTorr at 300 K). From Fig. 15, the design window is then extremely small, effectively ruling out the use of a chamber gas. As part of the R&D effort on target injection and survival, possible ways to make the target more thermally robust are being investigated, such as reducing the initial temperature perhaps to ~14 K, allowing some phase change and/or adding an insulated foam layer on the outside of the target [23]. These would help to accommodate higher chamber gas density (with the goal of 10's of mTorr), thereby significantly opening up the design window for armor survival and allowing for the possibility of higher yield and/or smaller chamber.

These example calculations illustrate the design analysis process whose results can be used as input in the overall system code to represent allowable sets of chamber operating parameters for a given fusion power.

7. Consideration of engineered tungsten armor

A major concern associated with fully dense tungsten armor is the possible accumulation of helium from ion implantation. Helium migration in tungsten is slow and the concern is that a build-up of helium could result in local armor failure. A possible solution is to minimize the migration distance of helium in the tungsten structure, which, coupled with the high temperature of operation, could help implanted helium migrate out of the structure. Such a fine structure could be part of a configuration with interconnected porosity, which would provide the helium a subsequent path of least resistance to the chamber. A simple analysis based on the diffusion coefficient for He in W from Wagner and Seidman [24] indicates that for a temperature of ≈1000–1500 K over a time of 0.1 s (corresponding to an example repetition rate of 10), the characteristic He diffusion length in W is about 10–50 nm. Higher temperature and/or longer times would help [3]. From these initial results, one should try to design an engineered structure with interconnected porosity and a micro-structure of dimension ≈10–100 nm. However, the behavior of implanted He in tungsten is a complex process involving a number of mechanisms and detailed modeling and experimental studies are required to better understand it and to design the armor accordingly (e.g. [25,26]).

Such a porous structure could also help in accommodating local thermal stresses and minimize possible lifetime-limiting mechanisms such as micro-crack formation and propagation and/or roughening. An important consideration in the development of such an engineered tungsten structure would thus be to provide a more stress-tolerant configuration with the capability to better accommodate the high armor heat flux. This would allow for operation under higher temperature levels and gradients.

Two possible engineered tungsten structures have been proposed as armor candidates: a high porosity foam proposed by Ultramet which is described in detail in Ref. [2]; and a nano-sized homogeneous porous region proposed by PPI whose initial thermal performance analysis is summarized below [3]. The overall configuration consists of a porous W layer over a fully dense W layer which is bonded to a ferritic steel structure representing the first wall of an IFE chamber. PPI proposes to use a vacuum plasma spray forming technique to manufacture such a layered structure with a functional gradient when transitioning from fully dense W to ferritic steel.

The thermal analysis of this engineered armor/FW configuration was performed by first estimating the energy deposition from the photon and ion threat spectra for the example 154 MJ direct-drive target. The calculation procedure is similar to that described in Section 2 but takes account of the lower density of the armor material. The effect of the porosity of the engineered armor on the ion energy deposition is illustrated in Fig. 16 for a 10-μm thick porous W region. The figure shows the ion energy deposition as a function of penetration depth for various engineered region porosities for the 154 MJ direct-drive target spectra assuming a chamber radius of 7.5 m and no protective gas in the chamber (consistent with the example parametric study presented in the previous section). From the figure, the maximum energy deposition decreases and the energy penetration depth increases with increasing porosity of the porous layer. This is to be expected since the ions deposit their energy deeper in the material as the W porosity increases.

The thermal calculations were performed using the modified RACLETTE code [14] and utilizing as input the previously calculated volumetric heat generation as a function of time and depth. For these scoping calculations of a W porous layer, the thermal conductivity of the porous region was scaled to its density. Typical results are summarized in Fig. 17 that shows the maximum temperature of the engineered tungsten surface as a function of the porous region thickness for different porosity values. From the results, the maximum armor temperature

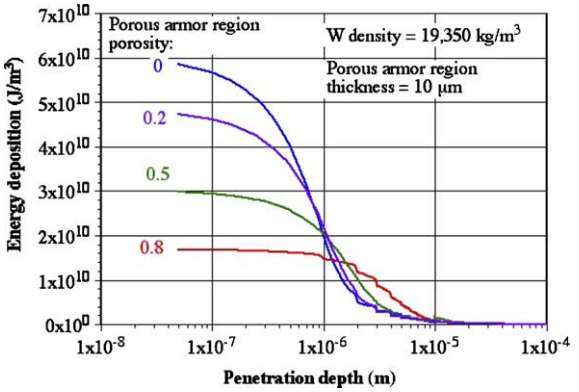

Fig. 16. Example ion energy deposition as a function of penetration depth for a W armor with a 10-μm porous layer subject to the 154 MJ direct-drive target threat spectra in a chamber of radius 7.5 m.

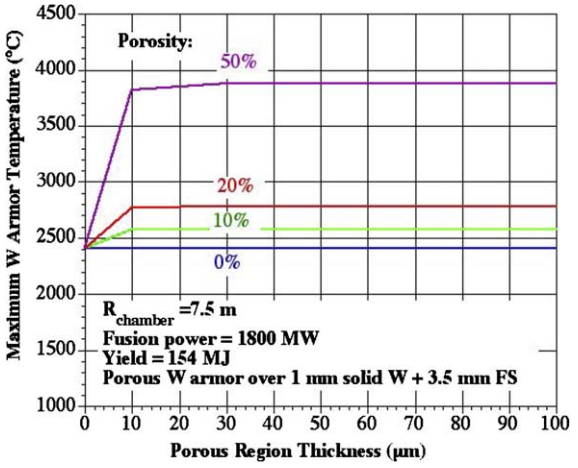

Fig. 17. Maximum W armor temperature as a function of the porous region thickness for different porosities of this region, for the 154 MJ direct-drive target and a chamber of radius 7.5 m. The assumed thicknesses of the fully dense W layer and of the ferritic steel structure are 1 mm and 3.5 mm, respectively and the assumed coolant temperature is 572 °C.

increases appreciably with increasing porosity of the porous region; it increases also with increasing porous region thickness but only up to a thickness corresponding to the ion penetration depth (<10 μm); increasing the porous region thickness past this has virtually no effect on the maximum armor temperature.

There are two porosity-dependent, competing mechanisms affecting the W porous region temperature rise: (i) increasing the porosity lowers the maximum energy deposition while spreading it spatially (see Fig. 16) which tends to reduce the maximum W armor temperature; and (ii) increasing the porosity lowers the thermal conductivity of the porous region which tends to result in higher armor temperature. Of these two, the later seems to have a stronger effect judging from the results in Fig. 17. These results indicate that it is important to minimize the porosity of the porous region (<≈20% if possible) but that there is some flexibility in setting its thickness. In addition, the presence of a porous region exposed to the energy deposition might help in better accommodating the thermal stresses on the armor, thereby allowing for higher maximum temperature limits and better armor survival. However, this would need to be verified by further R&D.

8. Conclusions

The HAPL laser IFE community has decided to concentrate on a first wall concept based on tungsten as armor material and ferritic steel as structural material. This allows for the possible use of a number of compatible blanket designs that are being developed for MFE. The major armor and first wall challenges include armor material type (e.g. W alloy and possible engineered structure), bonding to the low-activation ferritic steel, lifetime and general suitability of W/FS in an overall fusion/nuclear system. These issues are being addressed through the HAPL R&D program.

Results from the thermal analysis of the armor indicate that only a very thin armor region undergoes major temperature swings during operation. Consequently, the preferred design emphasizes separation of functions, with a thin armor providing the high energy accommodation function bonded to a FS substrate providing the structural function and interfacing with the coolant and blanket (which operate under quasi-steady-state conditions). Several considerations must be balanced in setting the armor region thickness; it must be set in coordination with the coolant temperature and film drop to ensure that the maximum temperatures of the FS and W stay within their respective allowable limits; it must also be set to maintain the temperature swing at the FS/W interface at an acceptable level; finally, the selected armor thickness needs to be compatible with demonstrated fabrication methods.

Example design window calculations were performed to illustrate how different chamber parameters can be set to meet certain constraints, such as the maximum W and FS temperature limits. For a given blanket and coolant configuration, the FS temperature limit would dictate the coolant conditions (temperature and convective heat transfer coefficient) in the first wall channel for a given fusion power level. Under these conditions, combinations of chamber size, target yield and protective chamber gas density can be derived that would accommodate the maximum W temperature constraint for a given armor/FS configuration. Such a parameter space has been calculated and shown for an example case with a fusion power of 1800 MW. Additional constraints from laser focusing and, more importantly, target survival requirements on chamber gas density must be included to develop the operating design window. For the base target (shown in Fig. 1), survival requirements based on preventing DT from reaching its triple point are very restrictive, effectively ruling out the possibility of any protective chamber gas. However, efforts are underway to develop a more thermally

robust target which could significantly open up the design window.

Lifetime-limiting processes are key issues for the armor; these include accumulation of implanted ions (in particular He whose diffusion in W is very slow) and thermal-stress driven processes such as roughening and crack propagation. Development of an engineered armor might help address these issues; for example, a porous armor with nano-sized structure and interconnected porosity would minimize the migration distance of helium in the tungsten structure which coupled with the high temperature of operation could help implanted helium migrate out of the structure. Such a porous configuration might also better accommodate local thermal stresses and restrain the associated lifetime-limiting processes. The thermal analysis of such a porous W armor bonded to a fully dense W layer which is itself bonded to a FS first wall indicates that it is important to minimize the porosity of the porous region ($<\approx 20\%$ if possible) but that there is some flexibility in setting its thickness. The R&D armor effort includes further investigation in developing such engineered material for armor application.

In conclusion, although some major issues still need to be resolved, the analyses show encouraging results for the possibility of utilizing a W-armored chamber in combination with a laser-driven direct-drive target. The major chamber armor and wall issues have been identified and are being addressed through a combination of modeling and experimental R&D. The effort on blanket and system is progressing in parallel with the goal of finding integrated design windows for a laser IFE power plant.

Acknowledgement

This work was supported by a grant from the Naval Research Laboratory, award no. N00173-01-1-G906.

References

[1] J. Sethian et al., J. Nucl. Mater. these Proceedings, doi:10.1016/j.jnucmat.2005.08.019.
[2] S. Sharafat, J. Nucl. Mater. these Proceedings, doi:10.1016/j.jnucmat.2005.08.012.
[3] 'Tungsten for IFE dry chamber walls', presented by S. O'Dell at the February 2004 HAPL meeting. Available from: <http://aries.ucsd.edu/HAPL/MEETINGS/0402-HAPL/program.html>.
[4] S.E. Bodner, G. Colombant, A.J. Schmitt, M. Klapisch, Phys. Plasmas 7 (6) (2000) 2298.
[5] D.T. Goodin, N.B. Alexander, C.R. Gibson, A. Nobile, R.W. Petzoldt, N.P. Siegel, L. Thomson, Nucl. Fusion 41 (2001) 527.
[6] Available from: <http://aries.ucsd.edu/ARIES/WDOCS/ARIES-IFE/SPECTRA/>.
[7] A.R. Raffray et al., ARIES Team, Fusion Sci. Technol. 46 (November) (2004) 417.
[8] I.N. Sviatoslavsky et al., Fusion Technol. 21 (1992) 1470.
[9] HAPL chamber tasks coordination document, 2004. Available from: <http://aries.ucsd.edu/HAPL/DOCS/>.
[10] See 'IFE materials response: long-term exposure to nitrogen and helium beams on RHEPP', presented by T. Renk, T. Tanaka; and 'BUCKY Simulations of Tungsten RHEPP Experiments: Initial Temperature, Ion Type Effects and Stresses', presented by R.P. Peterson, High Average Power Laser Meeting, Madison, WI, September 2003. Available from: <http://aries.ucsd.edu/HAPL/MEETINGS/0309-HAPL/ program.html>.
[11] S. Zinkle, N.M. Ghoniem, Fusion Eng. Des. 51&52 (2000) 55.
[12] Available from: <http://aries.ucsd.edu/LIB/PROPS/PHOTON/>.
[13] Available from: <http://www.srim.org/>.
[14] A.R. Raffray, G. Federici, J. Nucl. Mater. 244 (1997) 85; See also, G. Federici, A.R. Raffray, J. Nucl. Mater. 244 (1997) 101.
[15] R.R. Peterson et al., Fusion Technol. 30 (1996) 783.
[16] D. Haynes, private communication, 2003.
[17] R. Schleicher, A.R. Raffray, C.P. Wong, Fusion Technol. 39 (2) (2001) 823.
[18] A.R. Raffray, M. Akiba, V. Chuyanov, L. Giancarli, S. Malang, J. Nucl. Mater. 307–311 (2002) 21.
[19] I. Sviatovslasky, R. Raffray, M. Sawan, X. Wang, Fusion Sci. Technol. 47 (3) (2005) 535.
[20] See 'Preliminary parametric analysis of first wall, blanket and cycle for HAPL Power Plant', presented by A.R. Raffray at the HAPL September 2003 meeting. Available from: <http://aries.ucsd.edu/HAPL/MEETINGS/0309-HAPL/program.html>.
[21] F. Najmabadi, A.R. Raffray, et al., Fusion Sci. Technol. 46 (November) (2004) 401.
[22] R.W. Petzoldt et al., Nucl. Fusion 42 (2002) 1351.
[23] A.R. Raffray, R. Petzoldt, J. Pulsifer, M.S. Tillack X. Wang, Fusion Sci. Technol. 44 (1) (2003) 111.
[24] A. Wagner, D.N. Seidman, Phys. Rev. Lett. 42 (1979) 515.
[25] N.R. Parikh et al., J. Nucl. Mater. these Proceedings, doi:10.1016/j.jnucmat.2005.08.017.
[26] B.B. Cipiti, G.L. Kulcinski, J. Nucl. Mater. these Proceedings, doi:10.1016/j.jnucmat.2005.08.009.